Check for updates

Silicon photonics interfaced with integrated electronics for 9 GHz measurement of squeezed light

Joel F. Tasker[1,4], Jonathan Frazer[1,2,4], Giacomo Ferranti [1], Euan J. Allen[1], Léandre F. Brunel[3], Sébastien Tanzilli [3], Virginia D'Auria[3] and Jonathan C. F. Matthews [1✉]

Photonic quantum technology can be enhanced by monolithic fabrication of both the underpinning quantum hardware and the corresponding electronics for classical readout and control. Here, by interfacing complementary metal–oxide–semiconductor (CMOS)-compatible silicon and germanium-on-silicon nanophotonics with silicon-germanium integrated amplification electronics, we curtail total capacitance in a homodyne detector to enhance the speed performance of quantum light measurement. The detector has a 3 dB bandwidth of 1.7 GHz, is shot-noise limited to 9 GHz and has a minaturized required footprint of 0.84 mm². We show that the detector can measure the continuous spectrum of squeezing from 100 MHz to 9 GHz of a broadband squeezed light source pumped with a continuous-wave laser, and we use the detector to perform state tomography. This provides fast, multipurpose, homodyne detectors for continuous-variable quantum optics, and opens the way to full-stack integration of photonic quantum devices.

Silicon photonics is emerging as a sophisticated chip platform to develop quantum technology. It is being used to realize general-purpose programmable networks to process quantum states generated on-chip, with hundreds of individual components[1], as well as more specific tasks such as quantum random number generation[2] and chip-to-chip quantum communications[3]. However, classical interface hardware for integrated quantum photonics is still being implemented with large-footprint discrete electronics that limit device scalability and performance; silicon quantum photonics is yet to exploit integration with monolithic complementary metal–oxide–semiconductor (CMOS) electronics. Fully exploiting CMOS compatibility is of particular importance for reducing the total device footprint and where high-performance classical control and readout resources must scale with underpinning quantum hardware. Together, this enables miniaturization and mass manufacture of small quantum devices—for communication[4], sensing[5] and generating randomness[6]—and promises the precision and scale of fabrication required to assemble useful quantum computers [7].

Homodyne detectors measure weak signals by interference with a local oscillator that is detected by two balanced photodiodes. They are routinely used for sensitive measurement of light. Applications include coherent Ising machines[8], dual-comb spectroscopy[9], quantum-secured communication[3], quantum-state and process tomography[10], quantum computing[11], random number generation[12], quantum teleportation[13] and ultrasensitive interferometry, such as gravitational wave astronomy[14,15]. Homodyne detectors are also needed for recently proposed optical neural networks performing below the Landauer limit[16]. But in many applications, the speed performance is limited by the picofarad capacitance of non-monolithic electronic circuits and the maximum speeds of vertically illuminated photodiodes[17]. In particular, detector bandwidth can define the clock rate of continuous-variable (CV) quantum computers[18,19] and the secure-key exchange rate for CV quantum communications[3]. In addition, higher-speed homodyne detectors can vastly reduce the time needed to characterize pulsed quantum states or eliminate the need for long delay lines in heralded preparation of states[20], and could be used to measure high-frequency combs of squeezing from optical cavities[21] and broadband squeezing generated with continuous-wave (CW) pumps[22].

PIN photodiodes suffer from excess loss at frequencies above the transit-time roll-off due to distributed absorption in the photodiode intrinsic region[17]. This effect is pronounced in vertically illuminated diodes because a thick intrinsic region is required to achieve high quantum efficiency, leading to long transit times and excess loss, which increases with frequency above 100 MHz (Si) and 1 GHz (InGaAs)[17]. As waveguide-coupled Ge photodiodes are edge coupled, high efficiencies can be achieved by increasing the diode length, without increasing the transit-time-limited bandwidth. High-efficiency Ge photodiodes have been demonstrated with transit-time-limited bandwidths in excess of 70 GHz (ref. [23]) and thus suffer no effective loss from distributed absorption over this frequency range.

The speed performance of homodyne detectors is also limited by that of the transimpedance amplifiers (TIAs) used to amplify the weak photocurrent subtraction of the two photodiodes with low noise, to measure weak signals including quantum signatures[10]. The 3 dB bandwidth of an ideal Butterworth response TIA—employing a voltage amplifier with gain–bandwidth product $A_0 f_0$ and a shunt-feedback resistor R_F—is given by[24] $f_{3dB} = \sqrt{\frac{A_0 f_0}{2\pi R_F C_{Tot}}}$. For a given amplifier technology and gain R_P f_{3dB} can be increased only by reducing C_{Tot}, which is the sum of the photodiode junction
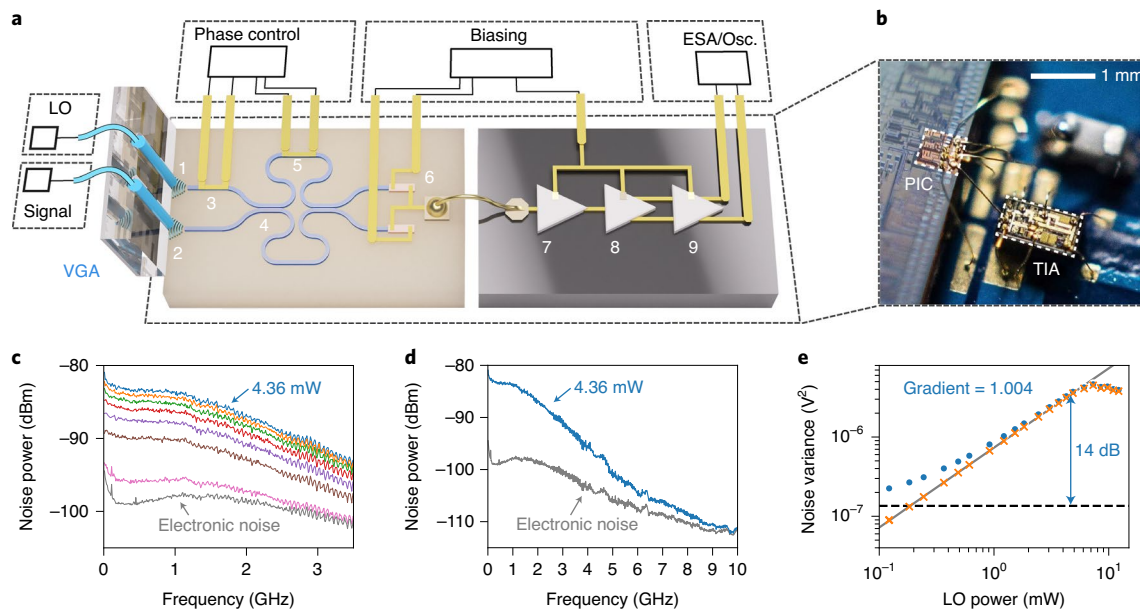
Fig. 1 | Device schematic and characterization. a, Illustration of the PIC and TIA. See Results section for details of labels 1–9. The homodyne signal is recorded with an electronic spectrum analyser (ESA) and oscilloscope (Osc.). **b**, Photograph of the homodyne detector device mounted onto a PCB. **c**, Spectral response, with 100 kHz resolution bandwidth, of the detector with increasing LO powers from bottom to top in the range {0 mW, 0.12 mW, 0.85 mW, 1.58 mW, 2.30 mW, 3.00 mW, 3.69 mW, 4.36 mW}, corrected for PIC insertion loss. **d**, Spectral response of detector across 10 GHz of spectrum analyser bandwidth. **e**, Raw (dots) and electronic-noise-subtracted (crosses) signal variance with different CW LO powers integrated over a bandwidth of 1.7 GHz. The black line represents the noise floor of the detector. The grey line is fitted over all but the last five data points where the photodiodes begin to saturate—the gradient of this line on the bi-logarithmic scale is 1.004 ± 0.003.

capacitances, amplifier input capacitance, and total parasitic capacitance of the amplifier input and feedback loop. In principle, C_{Tot} can be very low; integrated photodiodes can reach capacitances as low as 9 fF (ref. [23]) while amplifiers can have input capacitances of the order of 100 fF (ref. [25]). However, for shot-noise-limited applications, the integrated photonics approach—that has only been used to measure vacuum and laser light—has so far not exceeded 150 MHz (refs. [2,3]), which is far below the of order 1 GHz bandwidths achievable with free-space photodiodes[26]. This is because the TIAs have been implemented with packaged amplifiers and printed circuit boards (PCBs). For integrated homodyne detectors utilizing PCB-based TIAs, the parasitic capacitance of the PCB circuit alone can be ~215 pF (refs. [2,24]) while packaged operational amplifiers typically have input capacitances of several picofarad[2]. C_{Tot} is thus dominated in these cases by parasitic effects, negating the advantage of integrated photodiodes. Furthermore, as the frequency-dependent noise power of the circuit is proportional to $C_{TOT}^2 f^2$ (ref. [24]), this stray capacitance also strongly limits the shot-noise clearance achievable at high frequencies.

Results

Our homodyne detector is illustrated in Fig. 1 and implements, in a silicon photonic integrated circuit (PIC) chip architecture, all the integrated linear optics[27] together with on-chip photodiodes[2] needed for a standard homodyne detector. The PIC is designed in-house and fabricated by IMEC Foundry Services[28]. A laser used as a local oscillator (LO)—used to extract phase information from a signal field—is guided into 450×220 nm single-mode waveguides via a fibre v-groove array (VGA) into a vertical grating coupler before input (1). The loss due to each grating coupler is −2.1 dB. The signal measured is input into (2). The phase between signal and LO is controlled with a thermal phase shifter (3) and the two fields interfere at a beamsplitter implemented with a variable Mach–Zehnder interferometer (MZI) comprising two directional

couplers (4) and a second thermal phase shifter (5) to precisely tune reflectivity. The wavelength range of this device is limited by the grating couplers, which have a measured 1 dB bandwidth of approximately 42 nm centred at 1,562 nm (Supplementary Section 11). The target photodiode efficiency is flat across the c-band. The chip exhibits cross-talk between the LO and MZI phase shifters of approximately 0.9%, which is mitigated by locking the MZI to 50% reflectivity using a PID feedback routine (see Supplementary Section 6 for details). Two waveguide-integrated germanium photodiodes (6)—approximately 100 μm in length with foundry target quantum efficiency of 87.6% (responsivity of 1.1 A W^{-1} at 1,560 nm) and 50 Ω bandwidths of 17 GHz—are coupled to the two outputs of the MZI. The two photodiodes are connected together in a balanced configuration on the metallization layer of the PIC with output ports accessed by bond pads. The PIC is wire bonded directly to an unpackaged commercial TIA die fabricated in a Si-Ge bipolar process with typical transimpedance gain of 3.3 kΩ (Supplementary Section 1). The die consists of an initial TIA stage (7), followed by a voltage amplifier (8) and output buffer amplifier (9). Direct interfacing is used to access the speed performance of the integrated photodiodes and the TIA by minimizing the parasitic capacitance and inductance at the input to the amplifier (Maxim Integrated). Both the PIC and the TIA die are mounted on a custom-designed PCB for biasing (Fig. 1b, and see Supplementary Section 1 for details).

The utility of a homodyne detector for quantum applications can be measured by its frequency response (including its ability to resolve the shot noise of a bright local oscillator field above the dark noise of the detector), common-mode rejection ratio (CMRR) and overall quantum efficiency. Characterization of the detector is performed with no light (vacuum) coupled to input (1). The frequency response and shot-noise clearance as a function of frequency determines the time mode of quantum states that may be accurately characterized by the detector—for our detector, this is shown in Fig. 1c,d. A common bandwidth metric is the 3 dB cutoff frequency
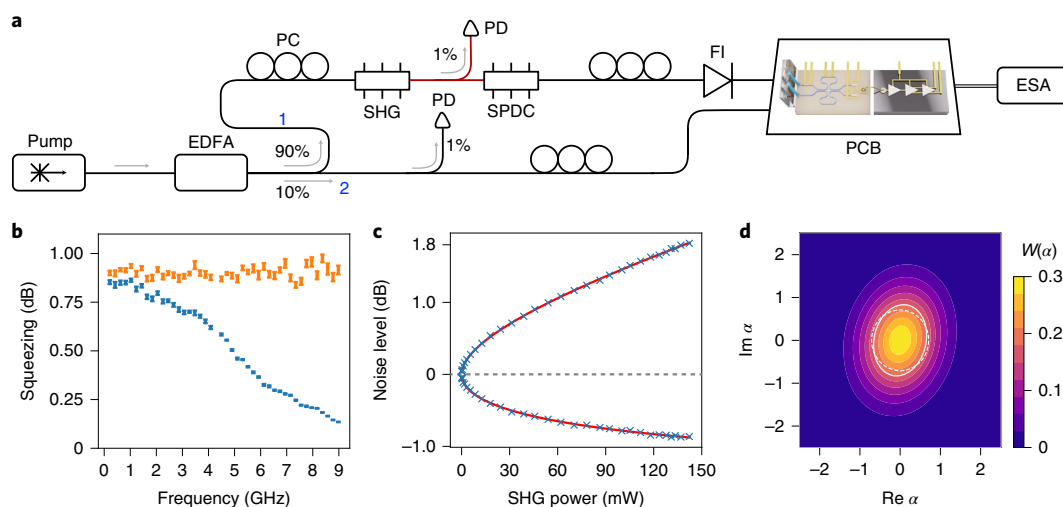
Fig. 2 | Measurement of a fibre-coupled squeezing source using the integrated detector. a, Experimental set-up. A tunable CW pump laser centred at 1,560.61 nm is amplified with an erbium-doped fibre amplifier (EDFA) before splitting into squeezing (1) and LO (2) paths. The polarization of the light in both paths is set (PC, polarization controller) to optimize SHG and squeezed light generation via SPDC, and PIC input coupling. Both SHG and SPDC are implemented with a PPLN ridge waveguide. Attenuation of the 90% path controls the SHG pump power independent of the LO. Power is monitored (PD, photodiode) in each arm with 99:1 fibre splitters. A fibre isolator (FI) acting as a filter suppresses residual 780 nm light. Noise powers are collected over 1 s with an ESA in zero-span mode set to 8 MHz resolution bandwidth. **b**, Measured squeezing levels across detector bandwidth with (orange) and without (blue) signal-to-noise ratio correction (see Supplementary Section 7 for method of estimation). We use the standard error of the data points as error bars. One data point has been removed at 4.29 GHz due to environmental radio-frequency interference. The drop in measured squeezing at higher frequencies is expected to be due to the reduction of shot-noise clearance, which adds an effective loss (Supplementary Section 8). **c**, Measured squeezing and anti-squeezing levels (blue crosses) with SHG power monitored using a 99:1 beamsplitter between PPLN modules. Equation (1) has been fit to find total detection efficiency η_{total} and μ (red line). Error bars are smaller than data points. **d**, Reconstructed Wigner function ($W(\alpha)$ with $\alpha = x + iy$, the optical phase space quadratures) of the squeezed vacuum integrated from 0 to 2 GHz. Solid and dashed white lines represent $W(\alpha) = 1/e$ contours of the squeezed and vacuum states, respectively.

of the shot noise; however, measurements can be made beyond this provided there is sufficient shot-noise clearance[29]. Accounting for frequency-dependent losses in the coaxial radio-frequency connecting cables, we obtain a 3 dB bandwidth of 1.7 GHz by fitting measured data with a Butterworth response (Supplementary Section 2). Figure 1d shows that shot noise can be measured above dark noise to 9 GHz.

The CMRR determines how well the photocurrent subtraction suppresses common-mode signals, such as classical laser amplitude noise. CMRR is set at d.c. by the accuracy of the beamsplitter reflectivity and matching of photodiode responsivities, but is degraded at higher frequencies by optical and electronic path-length imbalances[30]. The inherent mode matching of integrated optics, as well as the precise path-length matching afforded to integrated circuits, enables a high CMRR to be achieved through the tuning of a single thermal phase shifter. By amplitude modulating the LO and varying the MZI between balanced and unbalanced configurations, we measure a CMRR of >52 dB at 1 GHz (we attribute this limit to the dynamic range of the detector—see Supplementary Section 3).

Quantum efficiency is determined by losses in the detector's optics, the efficiency of the photodiodes and its shot-noise clearance. We cannot probe the individual photodiode efficiencies without the presence of coupled waveguides, so instead measure the combination of optical loss and efficiency to be $\eta_{det} \approx 8\%$ (Supplementary Section 4). To measure the shot-noise clearance of our detector and verify that the photocurrent noise increases in power linearly with the LO power—a signature that the detector is shot-noise limited—we plot the variance of the detector output as a function of input power on a bi-logarithmic scale (Fig. 1e). In the linear, unsaturated regime, we obtain a maximum shot-noise clearance of 14 dB and noise-subtracted gradient of 1.004 ± 0.003. While this is lower than the up to 18 dB clearance achievable

with non-monolithic detectors[22,26], the 3 dB bandwidth we observe is greater than has so far been reported with non-monolithic detectors—for example, ref. [22] reports a 3 dB cutoff of 400 MHz, while ref. [26] reports 1.2 GHz. Our observed clearance gives an efficiency contribution of 96% and therefore a total quantum efficiency of the detector of $0.88 \times 0.96 = 84\%$ for measuring states guided in the PIC.

Many quantum optics applications involve measuring squeezed light and states derived from non-Gaussian operations[10]. We apply our device to measure broadband squeezed light generated from a commercially available fibre-coupled periodically poled lithium niobate (PPLN) ridge waveguide chip (Fig. 2a). The source[31] is composed of an amplified CW telecom pump laser, a second-harmonic generation (SHG) stage and a parametric downconverter (SPDC)—we launch the generated squeezed vacuum into the second input of the chip provided for the signal input. As reported in ref. [31], we expect the source to have 80 nm full-width at half-maximum bandwidth of squeezing, well beyond the bandwidth of our homodyne detector. Figure 2b shows the measured squeezing across the full detector bandwidth, directly observing an average of 0.84 ± 0.03 dB of squeezing over the 3 dB bandwidth. It is still possible to extract meaningful quantum light properties beyond this with our device[29]. Subtracting calibrated electronic noise, we retrieve the post-noise-calibrated measurement of squeezing up to 9 GHz plotted in Fig. 2b. To measure the squeezing and anti-squeezing shown in Fig. 2c, the LO phase is scanned using the on-chip phase shifter (Supplementary Section 5) at 5 Hz. This is repeated for a range of SHG powers (directly monitored between modules). We fit the data with quadrature variances described by

$$\Delta X^2_{\substack{\text{MAX} \\ \text{MIN}}} = \eta_{\text{total}} \exp(\pm 2r) + (1 - \eta_{\text{total}}), \qquad (1)$$

with overall set-up efficiency η_{total} and $r = \mu\sqrt{P_{\text{SHG}}}$ (ref. [31]), for anti-squeezing (MAX) and squeezing (MIN). From this we obtain $\hat{\eta}_{\text{total}} = 0.28 \pm 0.01$ and $\mu = 0.044 \pm 0.002\,\text{mW}^{-1/2}$.

To account for the overall squeezing measurement efficiency, η_{total}, we identify all the sources of loss. From ref. [31] we assume ~0.83 transmission through the ridge waveguide and ~0.8 coupling between the SPDC module and output fibre, followed by 0.85 transmission measured through the fibre isolator, polarization controller and fibre couplers. The coupling into the photonic chip is measured to be −2.1 dB (= 0.62) per grating coupler and is monitored throughout the experiment. The measured photodiode quantum efficiency of $\eta_{\text{det}} = 88\%$ and shot-noise contribution of ~96% means the device acts as a fibre-coupled module with detection efficiency of 0.51, sufficient for CV quantum key distribution applications[3]. We estimate the overall detection efficiency of the squeezing experiment as $\eta_{\text{total}} \approx 0.292$, which is in close agreement to the fitted value of $\hat{\eta}_{\text{total}} = 0.28 \pm 0.01$. After correction for η_{total}, we estimate a squeezing value of 3.20 ± 0.21 dB at the SPDC module output.

To demonstrate the device's capability to reconstruct input quantum states with phase dependence, we perform homodyne tomography, on-chip, of the detected squeezed vacuum. Using the input thermal phase shifter (3 in Fig. 1), we scan the relative phase between LO and signal by applying a 100 Hz periodic voltage—faster than the slow thermal phase fluctuations arising in the fibres due to the environment—and acquire 2×10^7 phase-quadrature pairs over an integrated bandwidth of 2 GHz (see Supplementary Section 9 for more information). From these, we obtain a reconstruction of the quantum state by applying an iterative maximum likelihood estimation algorithm in a four-photon truncated Fock space[32]. The Wigner function of the reconstructed density matrix is shown in Fig. 2d.

Discussion

We have observed that low capacitance interfacing of the PIC with a micro-electronics TIA enables the speed performance to be greatly improved beyond that of previous PIC homodyne detectors[2,3] and the state-of-the-art non-monolithic homodyne detectors[22,26]. The achieved 3 dB bandwidth of 1.7 GHz is an order of magnitude greater than the previous reported integrated silicon-germanium demonstration[2,3] and a factor of 1.42 faster than the fastest reported free-space detector [26]. Our measurements of squeezed light up to 9 GHz indicate potential for using homodyne detectors to directly measure the quantum properties of light over wider bandwidths than can currently be achieved with non-monolithic photodiodes[22,26,29]. A heterogeneous or monolithic approach to further integrate optics with high-performance electronics could reduce parasitics to ~10 fF (ref. [25]) and enable bandwidths up to 100 GHz (Supplementary Section 10). This would both enhance existing CV quantum protocols and unlock integrated demonstrations of modalities such as feed forward and time multiplexing. In addition to the enhanced speed performance, the sub-mm² footprint is also of potential benefit, enabling the fabrication of arrays of homodyne detectors that could be used for measuring weak fields in multiple spatial modes.

Our improved fibre–chip coupling gives an overall efficiency improvement of a factor of 2.8 for detecting off-chip states, compared with previous PIC homodyne detectors[2]. This has assisted measurement of non-zero values of squeezing, showing the device could be used as a fibre-coupled detector module for quantum-enhanced measurements beyond the shot-noise limit of signals from 100 MHz to 9 GHz. Without further improvement, the device can be used with higher input levels of squeezing—for example, from calculating the impact of detector inefficiency, when using 6 dB of squeezing from a similar PPLN squeezing source[22] our device would measure ~2 dB of squeezing, while injecting 12 dB of squeezing[33], we would measure ~2.8 dB. Improved coupling to optical fibre is also possible—grating couplers have been shown[34]

to exceed 85% coupling efficiency using subwavelength photonic crystal structures and a metal mirror layer, while edge couplers have been demonstrated with 95% coupling efficiency[35].

The observed on-chip detection efficiency of 84% is an improvement of 40% above that of previously reported integrated homodyne detectors[2]. We expect a combination of reflection at the photodiode interface, as well as scattering and absorption in the metal contact regions, to limit the responsivity of the photodiodes that we use—furthermore, the geometry of these diodes have not been optimized for absorption. Prospects to improve detection efficiency are illustrated by integrated photodiodes reaching 95% efficiency with up to 30 GHz of bandwidth[36]. Recent demonstrations of squeezed light generation using ring resonators in silicon nitride[37–39] could be combined with the technology demonstrated here to generate and measure squeezed light within the same chip—multilayer Si/SiN fabrication with interlayer coupling efficiencies reaching −0.02 dB described in ref. [40] provides a promising approach to achieve this. By generating and detecting non-classical light on the same chip in this manner, and using the recent results of ref. [39], we expect ~4.8 dB of squeezing to be directly measurable with our current on-chip device efficiency.

Online content

Any methods, additional references, Nature Research reporting summaries, source data, extended data, supplementary information, acknowledgements, peer review information; details of author contributions and competing interests; and statements of data and code availability are available at https://doi.org/10.1038/s41566-020-00715-5.

References

1. Wang, J., Sciarrino, F., Laing, A. & Thompson, M. G. Integrated photonic quantum technologies. *Nat. Photon.* **14**, 273–284 (2019).
2. Raffaelli, F. et al. A homodyne detector integrated onto a photonic chip for measuring quantum states and generating random numbers. *Quantum Sci. Technol.* **3**, 025003 (2018).
3. Zhang, G. et al. An integrated silicon photonic chip platform for continuous-variable quantum key distribution. *Nat. Photon.* **13**, 839–842 (2019).
4. Gisin, N. & Thew, R. Quantum communication. *Nat. Photon.* **1**, 165–171 (2007).
5. Pirandola, S., Bardhan, B. R., Gehring, T., Weedbrook, C. & Lloyd, S. Advances in photonic quantum sensing. *Nat. Photon.* **12**, 724–733 (2018).
6. Herrero-Collantes, M. & Garcia-Escartin, J. C. Quantum random number generators. *Rev. Mod. Phys.* **89**, 015004 (2017).
7. Ladd, T. D. et al. Quantum computers. *Nature* **464**, 45–53 (2010).
8. McMahon, P. L. et al. A fully programmable 100-spin coherent ising machine with all-to-all connections. *Science* **354**, 614–617 (2016).
9. Millot, G. et al. Frequency-agile dual-comb spectroscopy. *Nat. Photon.* **10**, 27–30 (2016).
10. Lvovsky, A. I. & Raymer, M. G. Continuous-variable optical quantum-state tomography. *Rev. Mod. Phys.* **81**, 299–332 (2009).
11. Menicucci, N. C. et al. Universal quantum computation with continuous-variable cluster states. *Phys. Rev. Lett.* **97**, 110501 (2006).
12. Gabriel, C. et al. A generator for unique quantum random numbers based on vacuum states. *Nat. Photon.* **4**, 711–715 (2010).
13. Furusawa, A. et al. Unconditional quantum teleportation. *Science* **282**, 706–709 (1998).
14. Tse, M. et al. Quantum-enhanced Advanced LIGO detectors in the era of gravitational-wave astronomy. *Phys. Rev. Lett.* **123**, 231107 (2019).
15. Acernese, F. et al. Increasing the astrophysical reach of the Advanced Virgo detector via the application of squeezed vacuum states of light. *Phys. Rev. Lett.* **123**, 231108 (2019).
16. Hamerly, R., Bernstein, L., Sludds, A., Soljačić, M. & Englund, D. Large-scale optical neural networks based on photoelectric multiplication. *Phys. Rev. X* **9**, 021032 (2019).
17. Serikawa, T. & Furusawa, A. Excess loss in homodyne detection originating from distributed photocarrier generation in photodiodes. *Phys. Rev. Appl.* **10**, 064016 (2018).

18. Larsen, M. V., Guo, X., Breum, C. R., Neergaard-Nielsen, J. S. & Andersen, U. L. Deterministic generation of a two-dimensional cluster state. *Science* **366**, 369–372 (2019).

19. Asavanant, W. et al. Generation of time-domain-multiplexed two-dimensional cluster state. *Science* **366**, 373–376 (2019).

20. Zavatta, A., Viciani, S. & Bellini, M. Tomographic reconstruction of the single-photon fock state by high-frequency homodyne detection. *Phys. Rev. A* **70**, 053821 (2004).

21. Senior, R. et al. Observation of a comb of optical squeezing over many gigahertz of bandwidth. *Opt. Express* **15**, 5310–5317 (2007).

22. Kashiwazaki, T. et al. Continuous-wave 6-dB-squeezed light with 2.5-THz-bandwidth from single-mode PPLN waveguide. *APL Photon.* **5**, 036104 (2020).

23. Lischke, S. et al. High bandwidth, high responsivity waveguide-coupled germanium p-i-n photodiode. *Opt. Express* **23**, 27213–27220 (2015).

24. Masalov, A. V., Kuzhamuratov, A. & Lvovsky, A. I. Noise spectra in balanced optical detectors based on transimpedance amplifiers. *Rev. Sci. Instrum.* **88**, 113109 (2017).

25. Voki, N., Brandl, P., Schneider-Hornstein, K., Goll, B. & Zimmermann, H. 10 Gb/s switchable binary/PAM-4 receiver and ring modulator driver for 3-D optoelectronic integration. *IEEE J. Sel. Top. Quantum Electron.* **22**, 344–352 (2016).

26. Zhang, X., Zhang, Y.-C., Li, Z., Yu, S. & Guo, H. 1.2-GHz balanced homodyne detector for continuous-variable quantum information technology. *IEEE Photon. J.* **10**, 1–10 (2018).

27. Masada, G. et al. Continuous-variable entanglement on a chip. *Nat. Photon.* **9**, 316–319 (2015).

28. Rahim, A. et al. Open-access silicon photonics platforms in europe. *IEEE J. Sel. Top. Quantum Electron.* **25**, 1–18 (2019).

29. Ast, S. et al. Continuous-wave nonclassical light with gigahertz squeezing bandwidth. *Opt. Lett.* **37**, 2367–2369 (2012).

30. Painchaud, Y., Poulin, M., Morin, M. & Têtu, M. Performance of balanced detection in a coherent receiver. *Opt. Express* **17**, 3659–3672 (2009).

31. Kaiser, F., Fedrici, B., Zavatta, A., D'Auria, V. & Tanzilli, S. A fully guided-wave squeezing experiment for fiber quantum networks. *Optica* **3**, 362–365 (2016).

32. Lvovsky, A. I. Iterative maximum-likelihood reconstruction in quantum homodyne tomography. *J. Opt. B* **6**, S556 (2004).

33. Eberle, T. et al. Quantum enhancement of the zero-area sagnac interferometer topology for gravitational wave detection. *Phys. Rev. Lett.* **104**, 251102 (2010).

34. Ding, Y., Peucheret, C., Ou, H. & Yvind, K. Fully etched apodized grating coupler on the SOI platform with −0.58 dB coupling efficiency. *Opt. Lett.* **39**, 5348–5350 (2014).

35. Bakir, B. et al. Low-loss (<1 dB) and polarization-insensitive edge fiber couplers fabricated on 200-mm silicon-on-insulator wafers. *IEEE Photon. Technol. Lett.* **22**, 739–741 (2010).

36. Benedikovic, D. et al. 25 Gbps low-voltage hetero-structured silicon-germanium waveguide pin photodetectors for monolithic on-chip nanophotonic architectures. *Photon. Res.* **7**, 437–444 (2019).

37. Zhao, Y. et al. Near-degenerate quadrature-squeezed vacuum generation on a silicon-nitride chip. *Phys. Rev. Lett.* **124**, 193601 (2020).

38. Cernansky, R. & Politi, A. Nanophotonic source of quadrature squeezing via self-phase modulation. *APL Photon.* **5**, 101303 (2020).

39. Vaidya, V. D. et al. Broadband quadrature-squeezed vacuum and nonclassical photon number correlations from a nanophotonic device. *Sci. Adv.* **6**, eaba9186 (2020).

40. Hosseinnia, A. H., Atabaki, A. H., Eftekhar, A. A. & Adibi, A. High-quality silicon on silicon nitride integrated optical platform with an octave-spanning adiabatic interlayer coupler. *Opt. Express* **23**, 30297–30307 (2015).

Author contributions

J.F.T. and J.F. performed device characterization. J.F.T., J.F. and L.F.B. performed squeezed light measurements. J.F.T., J.F. and G.F. performed data analysis. All authors contributed to the theory, project direction and writing of the manuscript. J.C.F.M. directed the project.

Competing interests

The authors declare no competing interests.

Additional information

Supplementary information is available for this paper at https://doi.org/10.1038/s41566-020-00715-5.

Correspondence and requests for materials should be addressed to J.C.F.M.

Reprints and permissions information is available at www.nature.com/reprints.